

Modeling of nonphase mechanisms in ultrasonic modulation of light propagation

Quan Liu, Stephen Norton, and Tuan Vo-Dinh*

Departments of Biomedical Engineering and Chemistry, Duke University, Room 136,
Hudson Hall, Box 90281, Durham, North Carolina 27708-0281, USA

*Corresponding author: tuan.vodinh@duke.edu

Received 13 September 2007; revised 5 June 2008; accepted 6 June 2008;
posted 6 June 2008 (Doc. ID 87519); published 7 July 2008

While phase variation due to ultrasonic modulation of coherent light has been extensively studied in acousto-optical imaging, fewer groups have studied nonphase mechanisms of ultrasonic modulation, which may be important in exploring ultrasonic modulation of incoherent light for imaging. We have developed a versatile Monte Carlo based method that can model not only phase variation due to refractive index changes and scatterer displacement in tissue or tissue-like phantoms, but also amplitude and exit location variations due to the changes in optical properties and refractive index under ultrasonic modulation, in which the exit location variation has not, to the best of our knowledge, been modeled previously. Our results show that the modulation depth due to the exit location variation is three orders of magnitude higher than that due to amplitude variation, but two to three orders of magnitude lower than that due to phase variation for monochromatic light. Furthermore it is found that the modulation depth in reflectance due to the exit location variation is larger than that in transmittance for small source-detector separations. © 2008 Optical Society of America

OCIS codes: 290.1350, 290.4210, 290.7050, 170.3660, 110.7170, 000.4430.

1. Introduction

While pure three dimensional optical imaging, such as diffuse optical tomography, has shown great promise in differentiating cancerous lesions from normal tissue in a large tissue volume, it suffers from low spatial resolution [1]. Ultrasonic modulation was proposed to be incorporated into optical imaging to compensate for this weakness. This hybrid modality is often referred to as acousto-optical imaging. Since the early stages of this technique, phase variation due to ultrasonic modulation of coherent light has been extensively studied both theoretically and experimentally. For example, several authors have theoretically investigated the mechanisms of phase modulation [2–7]. Moreover, experiments have shown that this phenomenon can be used to image heterogeneities in a turbid medium [8–13]. In contrast, fewer groups have studied nonphase mechanisms of ultrasonic modulation,

although they may be important for exploring ultrasonic modulation of incoherent light for imaging. Mahan *et al.* [14] have studied the mechanism of intensity variation due to the modulation in the scattering coefficient but did not consider the mechanisms due to the modulation in the absorption coefficient and refractive index. Granot *et al.* [15] treated the ultrasonic modulation of photon propagation as a tagging process and derived an analytical formula relating the position of the ultrasound transducer to the optical signal at the detector, which could be applicable for both phase and nonphase variations. But one important parameter in the formula, the tagging efficiency, is not defined, so it is difficult to calculate the absolute modulation depth directly. Krishnan *et al.* [16] proposed a diffusion theory to model the ultrasonic tagging of fluorescence, which treats the refractive index gradient caused by ultrasonic modulation as an “acoustic lens” that diffracts fluorescent light. This theory did not consider the signal modulation caused by the variation in optical properties, which is another important mechanism.

Although it was previously stated that the ultrasonic modulation of incoherent light may be too weak to be experimentally observed [1], Kobayashi *et al.* [17] have recently shown that the ultrasonic modulation of fluorescent light can be observable in a carefully designed experiment, which suggests the potential of modulating other types of incoherent light, such as narrowband light, with ultrasound for optical imaging. To explore ultrasonic modulation of incoherent light for optical imaging, a versatile method that can model all known mechanisms in the ultrasonic modulation of light propagation, including both phase and nonphase variations, will be very useful. One important question this method will be able to answer is how large the modulation depth due to nonphase variations is compared with phase variations.

We have developed a Monte Carlo-based approach that can simulate both phase variation due to refractive index change and scatterer displacement as well as amplitude and exit location variations due to the changes in optical properties and refractive index, in which the exit location variation has not, to the best of our knowledge, been modeled previously. By simulating various mechanisms in a single Monte Carlo simulation, the modulation depth contributed by each mechanism can be fairly compared.

2. Methods

A. Principles of Amplitude and Exit Location Variation in Ultrasonic Modulation of Light Propagation

Ultrasonic modulation physically causes the compression and stretching of tissue components such as absorbers, scatterers, and surrounding medium, which consequently leads to the variation in the following parameters: the absorption and scattering coefficients and the refractive index. The amplitude, the phase, and the exit location of survival photons can all be affected by the variations in one or more of these parameters. Table 1 lists the known modulation mechanisms, all of which can be modeled by our method. The first column lists modulated tissue parameters that lead to the variations in light propagation parameters as listed in the middle column. The third column lists the relevant parameters that are directly related to measured field autocorrelation or light intensity. In the following sections the derivation will focus on the amplitude modulation and the exit location modulation, because they are less explored in the current literature. It is noteworthy to point out that

all variables that vary with ultrasonic modulation will be denoted by $\bullet(t)$ in the following subsections, where \bullet represents the variable.

1. Modulated Tissue Parameters

The change in the refractive index [18] at a point \vec{r}_j , which refers to the location of the j th collision, is

$$\Delta n(t) = n\eta k_a A \sin(\vec{k}_a \cdot \vec{r}_j - \omega_a t), \quad (1)$$

where n is the refractive index in the absence of ultrasonic modulation, η is a constant related to material properties and ultrasonic velocity [18], \vec{k}_a is the ultrasonic wave vector and k_a is the corresponding scalar, A is the ultrasonic amplitude that refers to the amplitude of the displacement of the medium in which ultrasound propagates, ω_a is the angular frequency of the ultrasonic wave, and t is time.

According to Beer's law [19], the absorption coefficient is proportional to the concentration of absorbers, i.e.,

$$\mu_a = 2.303 \cdot \sum_i \varepsilon_i C_i, \quad (2)$$

where μ_a is the absorption coefficient, ε_i is the molar extinction coefficient, and C_i is the concentration of the i th absorber. Because the change in concentration is synchronous with the ultrasound density wave, the change in the absorption coefficient would follow, which at point \vec{r}_j can be expressed as

$$\Delta\mu_a(t) = \mu_a \delta_{1j}(t), \quad (3)$$

where μ_a is the absorption coefficient in the absence of ultrasonic modulation and

$$\delta_{1j}(t) = k_a A \sin(\vec{k}_a \cdot \vec{r}_j - \omega_a t). \quad (4)$$

It is assumed here that $k_a A \ll 1$.

The change in the scattering coefficient is more complicated, because it is related to both scatterer density and refractive index mismatch as follows:

$$\mu_s = \rho_s Q_s A_s, \quad (5)$$

where ρ_s is the volume density, Q_s is the scattering efficiency, and A_s is the geometric cross section. Because the sizes of most tissue scatterers are

Table 1. Mechanisms of Ultrasonic Modulation

Modulated Tissue Parameter	Modulated Light Propagation Parameter	Measurable Parameter
Refractive index	Optical path length	Phase
Scatterer displacement	Optical path length	Phase
Optical Properties (μ_a and μ_s) ^a	Total mean free path ($1/\mu_t$)	Exit location
	Albedo (μ_s/μ_t)	Amplitude
Refractive index	Deviation from the straight scattering direction	Exit location

^a μ_a is the absorption coefficient and μ_s is the scattering coefficient. μ_t is the total attenuation coefficient, which is defined as $\mu_a + \mu_s$.

considerably smaller than the acoustic wavelength, the change in the particle size is a secondary effect relative to the change in the spacing between the particles. Therefore the geometric cross section is assumed to be not changed with ultrasound. The change in the volume density simply follows the ultrasound density wave, which at point \vec{r}_j can be denoted as

$$\Delta\rho_s(t) = \rho_s\delta_{1j}(t), \quad (6)$$

where ρ_s is the volume density in the absence of ultrasonic modulation. Then

$$\rho_s(t) = \rho_s + \Delta\rho_s(t) = \rho_s[1 + \delta_{1j}(t)], \quad (7)$$

where $\rho_s(t)$ is the time varying volume density under ultrasonic modulation.

The scattering efficiency Q_s can be calculated by Mie theory for commonly seen tissue scatterers. The approximation to the Mie solution for spherical scatterers [20] gives

$$Q_s = 3.28x^{0.37}(n_r - 1)^{2.09}, \quad (8)$$

where $x = 2\pi r/(\lambda/n_{\text{med}})$ and $n_r = n_p/n_{\text{med}}$, r is the radius of the scatterer particle, λ is the wavelength of light, n_p is the refractive index of the scatterer particle, and n_{med} is the refractive index of the surrounding medium. This approximation is valid for $5 < x < 50$ and $1 < n_r < 1.1$, which covers a large range of tissue scatterers. Among the variables in Eq. (8), both n_p and n_{med} can change with ultrasonic modulation, which follows Eq. (1). It is assumed the refractive index change of the scatterer is equal to that of the medium, which could approximately represent the case of real tissue whose main component is water (other cases will be discussed in Section 4). Then n_r remains unchanged because the changes in the refractive index of the scatterer and the medium cancel out. The modulated refractive index of the medium can be expressed by

$$n_{\text{med}}(t) = n_{\text{med}} + \Delta n_{\text{med}}(t) = n_{\text{med}}[1 + \eta\delta_{1j}(t)], \quad (9)$$

where n_{med} refers to the refractive index in the absence of ultrasonic modulation. Plugging Eq. (9) into Eq. (8) and keeping first-order terms only yields

$$Q_s(t) = Q_s[1 + 0.37\eta\delta_{1j}(t)], \quad (10)$$

where Q_s is the scattering efficiency in the absence of ultrasonic modulation.

Now replacing the ultrasound-dependent terms in Eq. (5) with Eqs. (7) and (10) generates

$$\mu_s(t) = \rho_s(t)Q_s(t)A_s \approx \mu_s[1 + \delta_{1j}(t) + 0.37\eta\delta_{1j}(t)], \quad (11)$$

where μ_s is the scattering coefficient in the absence of ultrasonic modulation. So the change in the scattering coefficient at point \vec{r}_j is

$$\Delta\mu_s(t) = \mu_s[1 + 0.37\eta]k_a A \sin(\vec{k}_a \cdot \vec{r}_j - \omega_a t). \quad (12)$$

For simplicity, let

$$\gamma = 1 + 0.37\eta, \quad (13)$$

then

$$\Delta\mu_s(t) = \mu_s\gamma k_a A \sin(\vec{k}_a \cdot \vec{r}_j - \omega_a t). \quad (14)$$

2. Modulated Light Propagation Parameters

Now let us look at how modulation in the optical properties and the refractive index would change light propagation in a Monte Carlo simulation. First the modulation in the albedo changes weight attenuation at each random walk step and subsequently the exit weight of survival photons:

$$\begin{aligned} a(t) &= \frac{\mu_s + \Delta\mu_s(t)}{\mu_t + \Delta\mu_t(t)} = \frac{\mu_s[1 + \gamma\delta_{1j}(t)]}{\mu_t + [(\mu_a + \mu_s\gamma)\delta_{1j}(t)]} \\ &\approx a \cdot [1 + (\gamma - 1) \cdot (1 - a) \cdot \delta_{1j}(t)], \end{aligned} \quad (15)$$

where a is the albedo in the absence of ultrasonic modulation.

Assuming a photon experienced N collisions before exit, its exit weight would be

$$\begin{aligned} \prod_{j=1}^N [a(t)] &= a^N \cdot \prod_{j=1}^N [1 + (\gamma - 1) \cdot (1 - a) \cdot \delta_{1j}(t)] \\ &\approx a^N \cdot \left[1 + \sum_{i=1}^N (\gamma - 1) \cdot (1 - a) \cdot \delta_{1j}(t) \right]. \end{aligned} \quad (16)$$

Therefore the fractional change in the exit weight at each step is

$$\Delta w(t) = (\gamma - 1) \cdot (1 - a) \cdot \delta_{1j}(t). \quad (17)$$

It is clear that the change in the exit weight is proportional to $1 - a = \mu_a/(\mu_a + \mu_s)$. It should be pointed out that $\Delta w = 0$ according to Eq. (17) when $a = 1$ or $\gamma = 1$. The case of $a = 1$ suggests that ultrasound modulation has no effect on the exit weight of individual photons in nonabsorbing media via this mechanism. In the case of $\gamma = 1$, the relative changes in μ_a and μ_s are equal.

Second the modulation in the total attenuation coefficient changes the total mean free path and, subsequently, the step size of the photon random walk. According to Eqs. (3) and (14), the modulation in the total attenuation coefficient can be expressed as

$$\begin{aligned} \Delta\mu_t(t) &= \Delta(\mu_a + \mu_s)(t) \\ &= (\mu_a + \mu_s\gamma)k_a A \sin(\vec{k}_a \cdot \vec{r}_j - \omega_a t). \end{aligned} \quad (18)$$

Assuming a random number generated from uniform distribution $\xi \in [0, 1]$, the step size for a static total attenuation coefficient μ_t in the absence of ultrasonic modulation is $L = -\ln(\xi)/\mu_t$, i.e., $-\ln(\xi) = L \cdot \mu_t$. When the total attenuation coefficient varies with location \vec{r}_j under ultrasonic modulation, the step size equation should hold for every infinitesimal interval along the random walk step, i.e., $-\ln(\xi) \cdot ds/L' = ds \cdot \mu_t(s)$, where L' is the new step size, s represents the spatial location along this random step, and $\mu_t(s)$ is the total attenuation coefficient in the presence of ultrasonic modulation that is a function of the spatial location. Integrating both sides from 0 to L' yields

$$-\ln(\xi) = \int_0^{L'} \mu_t(s) ds = \int_0^{L'} [\mu_t + \Delta\mu_t(s)] ds. \quad (19)$$

Writing $\vec{k}_a \cdot \vec{r}_j$ as $k_a \cdot s \cdot \cos\theta_j$, where θ_j is the angle between k_a and r_j , in Eq. (18) and plugging into Eq. (19), then equating the right-hand side of Eq. (19) to $L \cdot \mu_t$ and solving for L' yields

$$\begin{aligned} \Delta L(t) = L' - L &= -2 \frac{\mu_a + \mu_s \gamma}{\mu_t} \delta_{2j}(t) \\ &= -2[1 + (\gamma - 1) \cdot a] \delta_{2j}(t), \end{aligned} \quad (20)$$

where

$$\begin{aligned} \delta_{2j}(t) &= A \sin\left(\vec{k}_a \cdot \vec{r}_{j-1} + \frac{k_a L \cos\theta_j}{2} - \omega_a t\right) \\ &\times \sin\left(\frac{k_a L \cos\theta_j}{2}\right) / \cos\theta_j. \end{aligned} \quad (21)$$

It should be noted that the first-order approximation was used in Eq. (21). To facilitate tracking the random walk, the change in the step size can be decomposed to the components in the x , y , and z axes, which can then be accumulated separately at every step of the random walk. The accumulation of the step size change with time at each step causes the modulation in the exit locations of survival photons.

Finally the modulation in the refractive index can create a refractive index gradient in the medium that can distort the light path that would be straight in the absence of ultrasonic modulation. Similar to the modulation of the total attenuation coefficient, eventually this will also lead to the modulation in the exit location of the photon. Let us consider a single step ending at $(0, 0, z)$ that would be straight for a

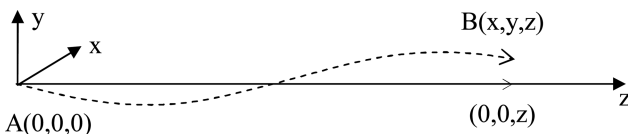


Fig. 1. A photon is assumed to start from $A(0,0,0)$ and travel along the z axis, which would end at $(0,0,z)$ for a uniform distribution of the refractive index. In the presence of a refractive index gradient, the photon path deviates from the straight line and ends at $B(x,y,z)$.

uniform distribution of refractive index as shown in Fig. 1. In the presence of a refractive index gradient, the photon path would deviate from the straight line and end at $B(x,y,z)$.

Assume

$$n(x,y,z) = n_0 + \epsilon h(x,y,z), \quad (22)$$

and introduce the displacements on the x and y axes,

$$x(z) = \epsilon f(z), \quad y(z) = \epsilon g(z), \quad (23)$$

where ϵ is a small constant related to ultrasound modulation, and $f(z)$ and $g(z)$ are two unknown functions that will be derived in the following steps:

Expanding $h(x,y,z)$ in a Taylor series to the first order, yields

$$\begin{aligned} n(x,y,z) &= n(\epsilon f, \epsilon g, z) = n_0 + \epsilon h(\epsilon f, \epsilon g, z) = n_0 \\ &+ \epsilon h_0(z) + \epsilon^2 f h_x(z) + \epsilon^2 g h_y(z) + o(\epsilon^3), \end{aligned} \quad (24)$$

where $h_0(z) = h(0,0,z)$, $h_x(z) = \partial h(x,y,z)/\partial x|_{x=0,y=0}$, and $h_y(z) = \partial h(x,y,z)/\partial y|_{x=0,y=0}$.

Plugging Eqs. (23) and (24) into the ray equations [21],

$$\begin{aligned} \frac{\partial n}{\partial x} \sqrt{x'^2 + y'^2 + 1} &= \frac{d}{dz} \left(\frac{nx'}{\sqrt{x'^2 + y'^2 + 1}} \right), \\ \frac{\partial n}{\partial y} \sqrt{x'^2 + y'^2 + 1} &= \frac{d}{dz} \left(\frac{ny'}{\sqrt{x'^2 + y'^2 + 1}} \right), \end{aligned} \quad (25)$$

the following equations can be obtained [22]:

$$n_0 \frac{d^2 f}{dz^2} = h_x(z), \quad n_0 \frac{d^2 g}{dz^2} = h_y(z). \quad (26)$$

Integrating Eq. (26) from 0 to z and applying $f(0) = g(0) = 0$ and $f'(0) = g'(0) = 0$ yields

$$\begin{aligned} f(z) &= \frac{1}{n_0} \int_0^z (z-z') h_x(z') dz', \\ g(z) &= \frac{1}{n_0} \int_0^z (z-z') h_y(z') dz'. \end{aligned} \quad (27)$$

Now turn to the coordinate system in the j th random walk step as shown in Fig. 2.

According to Eq. (1),

$$\begin{aligned} n(\vec{r}_j) &= n + n\eta k_a A \sin(\vec{k}_a \cdot \vec{r}_j - \omega_a t) \\ &= n + n\eta k_a A \sin[\vec{k}_a \cdot (\vec{r}_{j-1} + \vec{s}_j) - \omega_a t] \\ &= n + n\eta k_a A \sin[\vec{k}_a \cdot \vec{r}_{j-1} + \vec{k}_a \cdot \vec{s}_j - \omega_a t]. \end{aligned} \quad (28)$$

Comparing Fig. 2 with the coordinate system in Fig. 1, it is apparent that \vec{s}_j should be aligned with the z axis in Fig. 1 in the absence of ultrasonic modulation. To

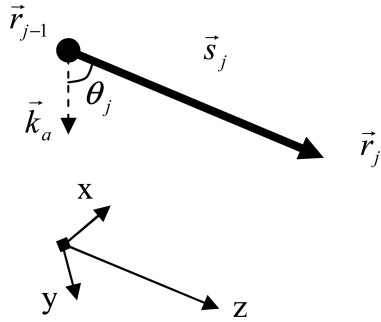


Fig. 2. Schematic of a photon step and the corresponding temporary coordinate system (x, y, z) for the calculation of x and y displacements due to ultrasonic modulation. \vec{r}_{j-1} is the start position and \vec{r}_j is the end position in the absence of ultrasonic modulation. $\vec{s}_j = \vec{r}_j - \vec{r}_{j-1}$, which makes an angle of θ_j with the ultrasonic wave vector \vec{k}_a . The $+z$ axis of the temporary coordinate system is aligned with \vec{s}_j and the x and y axes are arbitrarily chosen so that they are orthogonal to the z axis and to each other.

use Eq. (27) we need to first transform the original coordinate system so \vec{r}_{j-1} becomes the origin and \vec{s}_j points toward the $+z$ direction in the new coordinate system. This can be calculated by applying a coordinate transformation (see Appendix A). Assume \vec{k}_a becomes $\vec{k}'_a = [\vec{k}'_{ax}, \vec{k}'_{ay}, \vec{k}'_{az}]$ in the new coordinate system after the transformation, and an arbitrary point in the new system is denoted by $\vec{s}' = (x', y', z')$. Then, according to Eq. (28), the refractive index at this point can be rewritten as

$$\begin{aligned} n(\vec{s}') &= n + n\eta k_a A \sin[\vec{k}_a \cdot \vec{r}_{j-1} + \vec{k}'_a \cdot \vec{s}' - \omega_a t] \\ &= n + n\eta k_a A \sin[\vec{k}_a \cdot \vec{r}_{j-1} + \vec{k}'_{ax} x' \\ &\quad + \vec{k}'_{ay} y' + \vec{k}'_{az} z' - \omega_a t]. \end{aligned} \quad (29)$$

Comparing Eqs. (22) and (29), it is straightforward to know that

$$\begin{aligned} \varepsilon &= n\eta k_a A \quad \text{and} \quad h(x', y', z') \\ &= \sin[\vec{k}_a \cdot \vec{r}_{j-1} + \vec{k}'_{ax} x' + \vec{k}'_{ay} y' + \vec{k}'_{az} z' - \omega_a t]. \end{aligned} \quad (30)$$

Following the calculation procedure from Eq. (22) to Eq. (27), we can obtain the following results:

$$x'(z') = \varepsilon \vec{k}'_{ax} D(z'), \quad y'(z') = \varepsilon \vec{k}'_{ay} D(z'), \quad (31)$$

where $D(z') = -1 / (nk_{az}^2) [k'_{az} z' \sin(\Phi) + \cos(k'_{az} z' + \Phi) - \cos \Phi]$ and $\Phi = \vec{k}_a \cdot \vec{r}_{j-1} - \omega_a t$. Then the end position of this step becomes $\{x'(s_j), y'(s_j), s_j\}$, in which $s_j = |\vec{s}_j|$. These coordinates need to be transformed back to the x, y , and z displacements in the original coordinate system. Similar to the variation in the total mean free path, the deviation from the straight forward direction is accumulated at every step of the

random walk and eventually leads to the exit location modulation of survival photons. Interestingly the change in the physical length of this step due to the refractive index change is the second-order effect and thus can be neglected. However, the change in the optical path introduced by the refractive index variation is the first-order and thus cannot be neglected, which is one of the two primary mechanisms in phase modulation [18].

It should be pointed out that the first mechanism, i.e., albedo modulation, changes the exit weight of photons and thus should be theoretically observable for both finite-sized and infinitely large detectors. The latter two mechanisms rely on the change in the exit locations of survival photons and thus would not be observable for infinitely large detectors. Because the mean of the modulated fraction of outgoing light with respect to time is zero, it will be observable only if the light collection time is short relative to the ultrasonic period.

B. Monte Carlo Simulation

A Monte Carlo code [23] written for traditional light transport in multilayered media was modified to simulate light transport under ultrasonic modulation. Figure 3(a) illustrates the setup in simulations. It is clear that the setup is radially symmetrical about the incident beam. A few special steps were taken to speed up the Monte Carlo simulation. First the time-dependent variation in the exit weight or location was expressed as the summation of two products, in which the time-dependent terms and the time-independent terms are separated. For example, the fractional change in photon weight expressed by

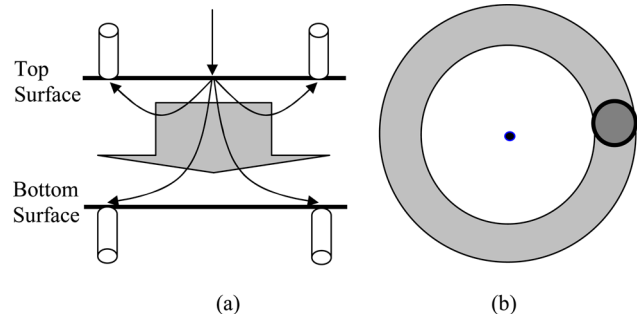


Fig. 3. (a) Setup in simulations. The bold horizontal lines represent the top and bottom surfaces of the tissue model. The two cylinders on the top surface are the circular detectors for detecting reflectance, while the two cylinders on the bottom surface are for detecting transmittance. The straight line with an arrow pointing at the top surface is a pencil incident beam. The four curved lines with arrows represent the trajectories of those photons detected on the top or bottom surfaces. The gray block arrow represents a planar ultrasound that travels downward. It can be seen that the setup is radially symmetrical about the incident beam. (b) The relation between a ring detector and the corresponding circular detector. The central dark spot is the source location, the light gray annular ring is the ring detector, and the dark gray circle with the bold line is the corresponding circular detector. The thickness of the ring detector is equal to the diameter of the corresponding circular detector.

Eq. (17) can be rewritten as

$$\begin{aligned}
 \Delta w &= (\gamma - 1) \cdot (1 - a) \cdot \delta_{1j} \\
 &= (\gamma - 1) \cdot (1 - a) \cdot k_a A \sin(\vec{k}_a \cdot \vec{r}_j - \omega_a t) \\
 &= (\gamma - 1) \cdot (1 - a) \cdot k_a A \sin(\vec{k}_a \cdot \vec{r}_j) \cos(\omega_a t) \\
 &\quad - (\gamma - 1) \cdot (1 - a) \cdot k_a A \cdot \cos(\vec{k}_a \cdot \vec{r}_j) \sin(\omega_a t) \\
 &= F_j \cdot \cos(\omega_a t) + G_j \cdot \sin(\omega_a t), \tag{32}
 \end{aligned}$$

where $F_j = (\gamma - 1) \cdot (1 - a) \cdot k_a A \sin(\vec{k}_a \cdot \vec{r}_j)$ and $G_j = -(\gamma - 1) \cdot (1 - a) \cdot k_a A \cos(\vec{k}_a \cdot \vec{r}_j)$. In the simulation, F_j and G_j , instead of Δw , were accumulated as a photon moves. After the simulation was finished, Eq. (32) was used to recover Δw at all time points. This approach eliminates the need of storing data for all time points during simulations and thus speeds up the simulations.

To reuse simulated data for a range of detector sizes and source-detector separation, the following information for each survival photon was recorded: the exit weight, the x and y values of the exit location, the x and y displacements due to the total attenuation coefficient modulation, and the x and y displacements due to the refractive index modulation. The numerical apertures of detectors were set such that all survival photons reaching the detectors would be counted regardless of their exit angles. It should be noted that both x and y displacements have been rewritten as in Eq. (32) so the data deposited for later use were the coefficients of $\cos(\omega_a t)$ and $\sin(\omega_a t)$ functions instead of the raw x and y displacements. Then the distance of the exit location of each survival photon from the incident location is used to determine whether the photon is collected by a ring detector. A scaling factor is calculated to determine the probability that it will be collected by the corresponding finite-sized circular detector. The relation between the ring detector and the corresponding circular detector is shown in Fig. 3(b). This approach is valid because the simulation setup as shown in Fig. 3(a) is radially symmetrical about the source location, which has been confirmed by comparing the phase modulation result with published data [5].

The optical properties of the tissue model were chosen to be representative of human tissue in the red spectrum as listed in Table 2. The thickness of

the tissue model was chosen to be a relatively small value (1 cm) to yield a sufficient number of photons for transmittance. The ultrasound traveled downward in a direction perpendicular to the top surface of the tissue model, and relevant parameters are listed in Table 2. Unless notified otherwise, the simulation was always run with one million incident photons for a total of ten runs. The results from all runs were averaged to generate the raw data for polynomial fitting in Subsection 2.C.

C. Polynomial Fitting of Modulation Terms for Finite-Sized Detector

One weakness of the Monte Carlo method is that it requires a large number of useful photons to minimize statistical uncertainty. When the number of useful photons is small, the result may not be meaningful. This is particularly true for investigating the ultrasonic modulation of the total attenuation coefficient and the refractive index. Because the changes in the exit location induced by these two mechanisms are usually tiny, the change in the number of survival photons collected by a finite-sized detector is close to zero as a consequence. To overcome this weakness, we use the following strategy: Consider a thin ring detector whose thickness is on the order of tens of micrometers. Count all photons that would reach this detector, take the average of the magnitude, the x and y displacements, and other quantities of interest for these photons, and use them as the representative values for the central position of the detector. Then vary the distance of this detector from the incident location, and calculate the representative values for a range of distances. Eventually those quantities of interest can be plotted as a function of the radial distance. A series of detector diameter, including 16, 32, 48, and 64 μm , that are comparable to the commonly used charge-coupled device pixel size [24] were tried, and it was found that the uncertainty in the result decreases with the increase in the detector diameter within this range, while the shapes of curves remain unchanged. Figure 4 shows the quantities of interest for the modulations of albedo, the total attenuation coefficient, and the refractive index as a function of the radial distance, which were calculated for diffuse reflectance (diffusely backscattered photons) simulated for a detector with a diameter of 64 μm . The curves for transmittance are more fluctuating.

Table 2. Optical Parameters and Ultrasonic Parameters Used in Simulations^a

Absorption Coefficient (μ_a , cm^{-1})	Scattering Coefficient (μ_s , cm^{-1})	Anisotropy (g)	Refractive Index Mismatch ^b	Thickness (cm)
0.1	10	0	1.1	1
Ultrasound Amplitude (cm)	Ultrasound Velocity (cm/s)	Frequency (Hz)	Material Property (η)	
1×10^{-8}	1.48×10^5	1×10^4 , 3.16×10^4 , 1×10^5 , 3.16×10^5 , 1×10^6 , 3.16×10^6 , 1×10^7	0.3211 ^c	

^aThe refractive index was fixed at 1.33 for all layers and surrounding media.

^bRefractive index mismatch refers to the ratio of the refractive index of scatterers to that of the surrounding medium.

^cThis value was calculated according to the parameters in Ref. [18].

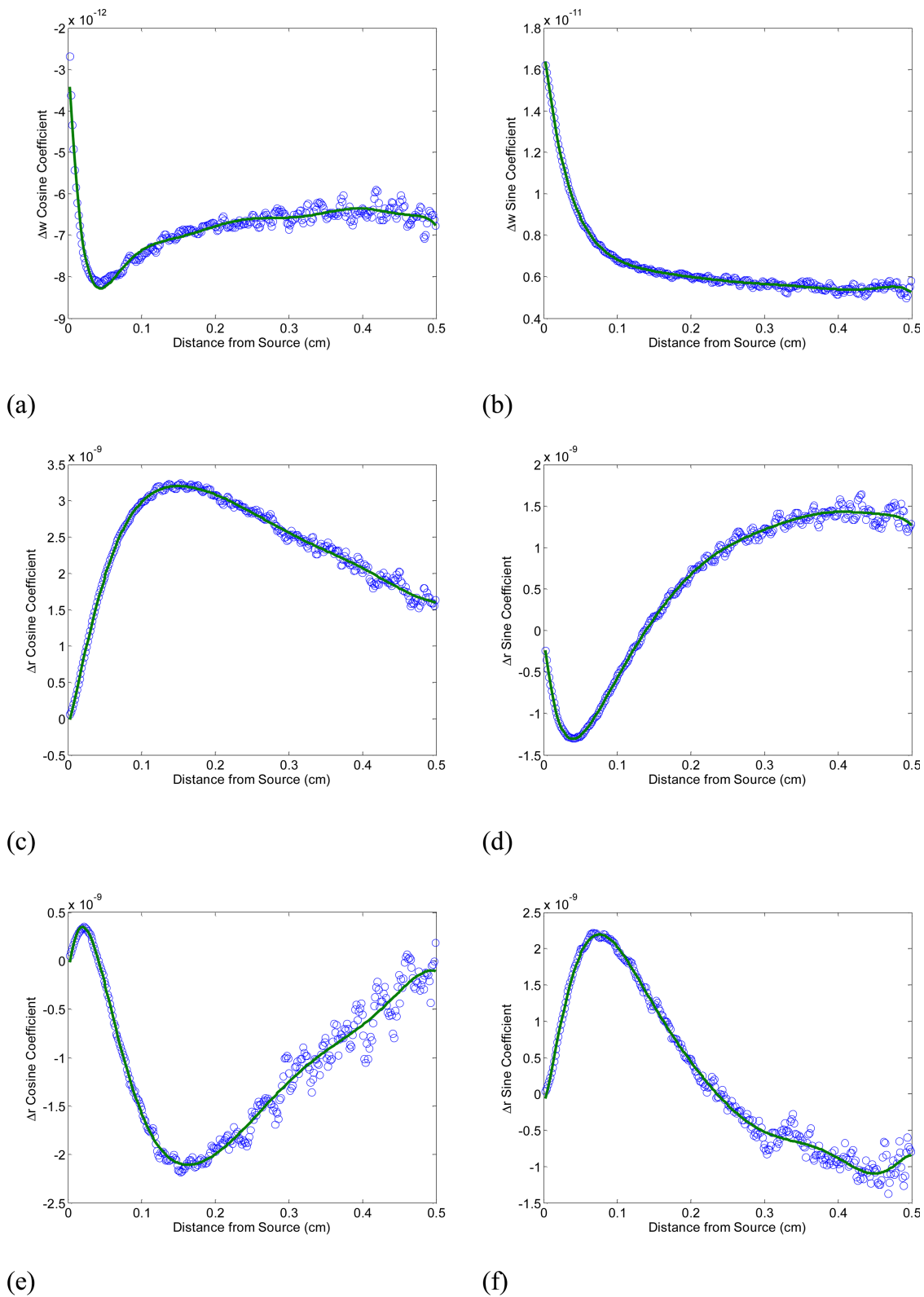


Fig. 4. (Color online) (a) $\cos(\omega_a t)$ coefficient and (b) $\sin(\omega_a t)$ coefficient in Δw (change in the exit weight) for albedo modulation; (c) $\cos(\omega_a t)$ coefficient and (d) $\sin(\omega_a t)$ coefficient in Δr (change in the exit radial distance) for total attenuation coefficient modulation; and (e) $\cos(\omega_a t)$ coefficient and (f) $\sin(\omega_a t)$ coefficient in Δr for refractive index modulation as a function of the radial distance, which was calculated for diffuse reflectance simulated for a detector with a diameter of $64 \mu\text{m}$ and an ultrasound frequency of 1 MHz. The circles are the simulated results, and the continuous curves represent the fitted polynomials. The units in (c)–(e) are in cm.

tuated, but the changes in the trends are similarly smooth.

Because these curves are smooth enough, just like the radial distribution of diffuse reflectance predicted by diffusion theory [25], polynomial curves can be fit to these data to remove the statistical uncertainty induced by the Monte Carlo method without loss of accuracy. It should be pointed out that the x and y displacements as a function of the radial distance are not smooth although the radial displacement is in Fig. 4.

D. Calculation of Intensity Modulation

Light intensity was chosen as the endpoint for calculating the modulation depth, because its modulation is observable for all three nonphase variation mechanisms. The procedure for calculating the modulated light intensity for all mechanisms is described in Appendix B. Because this approach only accounts for the modulation in the radial direction and ignores the modulation in its orthogonal direction, the modulation depth obtained this way would be smaller than the actual value but should be on the same order of magnitude. Using a circular detector would further artificially decrease the fraction of photons at the inner and outer radial edge that could contribute to intensity modulation and thus was not applied.

3. Results

Figure 5 shows the modulation depth as a function of ultrasonic frequency for the following mechanisms: Fig. 5(a) shows the amplitude variation due to albedo modulation; Fig. 5(b) shows the exit location variation due to the total attenuation coefficient modulation; and Fig. 5(c) shows the exit location variation due to refractive index modulation. The diameter of the circular detector [see Fig. 5(a)] or the radial thickness of the ring detector [see Figs. 5(b) and 5(c)] was fixed at $10\ \mu\text{m}$, and the source-detector separation was varied between 0.01, 0.05, and 0.2 cm. Several important findings need to be pointed out. First the modulation depths contributed by exit location variations due to the total attenuation coefficient and refractive index modulations are comparable. Furthermore, both of them are three orders of magnitude higher than that contributed by amplitude variation but two to three orders of magnitude lower than that due to phase variation (results not shown) for monochromatic light and finite-sized detectors. Second, while the amplitude modulation shows an increasing trend with ultrasonic frequency in Fig. 5(a), which is similar to the trend seen in a published phase modulation result [5], the other two mechanisms show a peak modulation depth between 1 and 10 MHz. Third the modulation depth generally tends to decrease with the increasing source-detector separation for the exit location modulation [see Figs. 5(b) and 5(c)].

Table 4 lists the modulation depths in reflectance and transmittance for the exit location modulations and two separations (one small and one large). The ultrasonic frequency was 1 MHz and the detector size

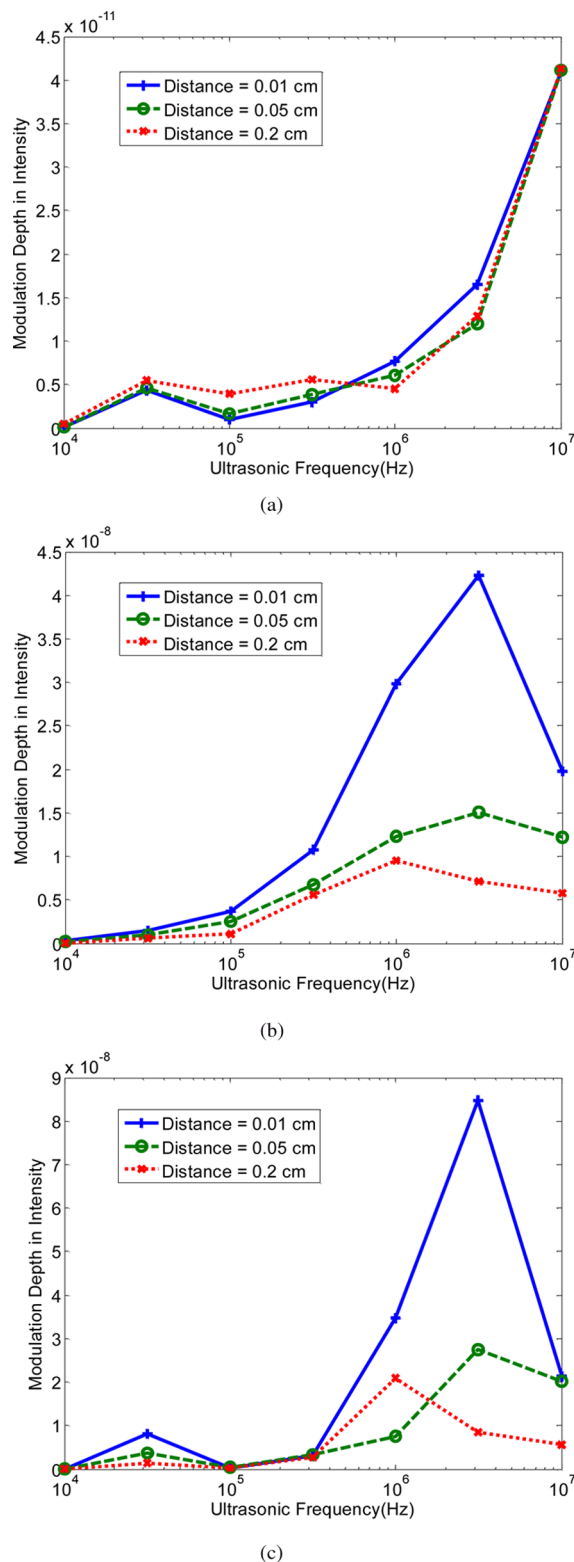


Fig. 5. (Color online) Modulation depth in intensity as a function of ultrasonic frequency for (a) amplitude variation due to albedo modulation, (b) exit location variation due to the total attenuation coefficient modulation, and (c) exit location variation due to refractive index modulation. The optical properties of the tissue model were kept unchanged in all simulations. Both the optical properties and ultrasonic properties are shown in Table 2. The diameter of the circular detector [in (a)] or the radial thickness of the ring detector [in (b) and (c)] was fixed at $10\ \mu\text{m}$.

was 10 μm . It can be seen that the modulation depth in reflectance is always larger than that in transmittance regardless of the source-detector separation.

4. Discussion

In the derivation of the modulated scattering coefficient as shown in Eq. (14), it was assumed that the refractive index change of the scatterer is equal to that of the medium, i.e., $\Delta n_p = \Delta n_{\text{med}}$. This special situation could approximately represent the case of real tissue whose main component is water. There are other cases in which the refractive index change of the scatterer is significantly different from that of the medium. For example, $\Delta n_p = 0$ might represent the case of using those particles with small compressibility relative to water (such as titanium dioxide) as the scatterer and water as the surrounding medium. $\Delta n_p = 2.17 \cdot \Delta n_{\text{med}}$ represents the case of using polystyrene spheres as the scatterer and water as the medium. These two cases correspond to two typically used scatterers in synthetic tissue phantoms. Table 4 lists the values of γ , Δw , and ΔL for these two cases as well as the case that has been previously calculated for real tissue.

Based on this table, it can be seen that the absolute values of Δw and ΔL for the cases of $\Delta n_p = 0$ and $\Delta n_p = 2.17 \cdot \Delta n_{\text{med}}$ are larger than for the case of $\Delta n_p = \Delta n_{\text{med}}$. As a result the modulation depth simulated for tissue phantoms where the scatterer is titanium dioxide ($\Delta n_p = 0$) or the scatterer is polystyrene spheres ($\Delta n_p = 2.17 \cdot \Delta n_{\text{med}}$) contributed by the mechanisms of amplitude modulation and the total attenuation coefficient modulation will be roughly proportionally larger than that simulated for real tissue ($\Delta n_p = \Delta n_{\text{med}}$) (data not shown). The modulation depth due to the refractive index modulation will remain unaffected.

It is demonstrated in Fig. 5(a) that the modulation depth due to amplitude modulation increases with ultrasonic frequency, which can be predicted from Eq. (17). Equation (17) clearly shows that the variation in the exit weight of survival photons is proportional to the ultrasonic wave number k_a and, in turn, the ultrasonic frequency. According to Figs. 5(b) and 5(c), the modulation depths contributed by the exit location variation due to the total attenuation coefficient modulation and the refractive index modulation are three orders of magnitude higher than that due to amplitude modulation. This can be explained by the fact that these two mechanisms are contributed by individual survival photons that per-

Table 4. Comparison in γ , Δw , and ΔL Between the Different Ratios of Δn_p and Δn_{med}

	$\Delta n_p = 0$	$\Delta n_p = 2.17 \cdot \Delta n_{\text{med}}$	$\Delta n_p = \Delta n_{\text{med}}$
γ	-6.26	9.73	1.12
Δw	$-0.072 \cdot \delta_{1j}(t)$	$0.086 \cdot \delta_{1j}(t)$	$0.0012 \cdot \delta_{1j}(t)$
ΔL	$12.38 \cdot \delta_{2j}(t)$	$-19.29 \cdot \delta_{2j}(t)$	$-2.24 \cdot \delta_{2j}(t)$

iodically switch the status from being detected to not being detected, which can be more significant than the weight change due to ultrasonic modulation if the total number of detected photons is small.

It is interesting to see that the modulation depths due to the exit location variations reach maxima at an ultrasonic frequency between 1 and 10 MHz, which is different from the trend in amplitude modulation. Although the reason is not intuitive, it is noticed that this is the zone where the mean transport free path is comparable with the ultrasonic wavelength.

Table 3 shows that the modulation depths in reflectance are always larger than those in transmittance for exit location variations. This can be explained by investigating a reciprocal problem. The modulation in the exit locations of survival photons, while keeping the detector fixed, is equivalent, to certain extent, to the modulation in the location of the detector, while keeping the exit locations of survival photons static. Then the modulated signal essentially depends on the difference in the first-order derivative of the collected signal as a function of the radial distance at the two edges of the detector, which is roughly equal to the second-order derivative for a small detector. For the small source-detector separations and optical properties shown in Table 2, the curve of reflectance as a function of the radial distance tends to have a larger second-order derivative than that of the transmittance as shown in Fig. 6. This infers that the modulation depths in reflectance due to exit location modulations should be larger than those in transmittance.

One potential pitfall of applying the method of polynomial fitting is that the raw data contributed by several photons with certain variability are replaced by a statistical mean. As a consequence the phenomena that are caused by higher-order statistics, such as variance, are not modeled. For this reason the results presented here should be used only for qualitative evaluation. In fact, an analytical model, which is based on a diffusion equation for the fluence of diffuse light in a medium with variable refractive index [26], has been developed in our group [27] to estimate the

Table 3. Modulation Depths in Reflectance and Transmittance for the Mechanisms of the Exit Location Variation and Two Separations (One Small and One Large)^a

	Exit Location Variation due to Total Attenuation Coefficient Modulation		Exit Location Variation due to Refractive Index Modulation	
	Separation = 0.01 cm	Separation = 0.2 cm	Separation = 0.01 cm	Separation = 0.2 cm
Reflectance	2.99×10^{-8}	9.55×10^{-9}	3.48×10^{-8}	2.10×10^{-8}
Transmittance	2.23×10^{-8}	2.97×10^{-9}	1.57×10^{-8}	9.33×10^{-9}

^aThe ultrasonic frequency was 1 MHz, and the detector size was 10 μm .

order of magnitude of the modulation depth for incoherent light due to refractive index variation. The modulation depth calculated from this analytical model is about one order of magnitude higher than that obtained from the Monte Carlo-based approach shown here for the optical and ultrasonic properties corresponding to an ultrasonic frequency of 1 MHz shown in Table 2. It is known [28] that the modulation depth of the overall detected signal α was related to the modulation depth of a single coherence area α_1 by $\alpha = \alpha_1/\sqrt{N}$, where N is the number of single coherence areas covered by the detector. Given the fact that the result from the analytical model is essentially for a single coherence area ($\sim 1\ \mu\text{m}$) while the result from the Monte Carlo-based approach is for a $10\ \mu\text{m}$ detector, the discrepancy between the two results is reasonably small.

Another important issue for the interpretation of the results in Fig. 5 is the valid range of the similarity relation, particularly for the diffuse reflectance results at small source-detector separations (distances of 0.01 and 0.05 cm). The reduced scattering

coefficient and $g = 0$ were used to generate a sufficient number of diffusely reflected photons for the calculation of reflectance. However, the anisotropy factor g is usually around 0.9 in real tissue. The equivalence of these two situations holds only for large source-detector separations for which photons have been multiply scattered upon detection. Therefore the absolute values of diffuse reflectance for small source-detector separations may not exactly represent the situations of real tissue, but the trend should be similar. The results of transmittance should be always accurate because transmitted photons would have to travel several transport mean free paths, and thus multiply scattered.

The proposed methodology can be easily adapted to other geometries. For example, when the light direction and ultrasound direction are orthogonal to each other, as those frequently used in relevant experiments, the axial symmetry is lost. In this case the displacements in both x and y dimensions instead of the radial displacement can be used to calculate the modulated signal.

As the bandwidth of light increases, the modulation depth due to phase modulation may change due to the loss of coherence; but the modulation depths due to amplitude modulation and exit location modulation should remain approximately unaf-

ected because they do not depend on the coherence property of light. It would be interesting to use the method developed to investigate for what light source nonphase modulation would be significant compared with phase modulation. The result would provide a theoretical guide to optimization of experimental setups for acousto-optical imaging with fluorescent light or other incoherent light. This is a future direction for this study.

Appendix A

The rotation of coordinates by a known angle about a known rotational axis can be expressed in several forms. According to the angle-axis representation [29], a rotation can be defined by a single angle of rotation, θ , and the direction of a unit vector, $\hat{n} = (x, y, z)$, about which to rotate. The transformation matrix is as follows:

$$M(\hat{n}, \theta) = \begin{bmatrix} \cos \theta + (1 - \cos \theta)x^2 & (1 - \cos \theta)xy - (\sin \theta)z & (1 - \cos \theta)xz + (\sin \theta)y \\ (1 - \cos \theta)xy + (\sin \theta)z & \cos \theta + (1 - \cos \theta)y^2 & (1 - \cos \theta)yz - (\sin \theta)x \\ (1 - \cos \theta)xz - (\sin \theta)y & (1 - \cos \theta)yz + (\sin \theta)x & \cos \theta + (1 - \cos \theta)z^2 \end{bmatrix}. \quad (\text{A1})$$

Now go to the special situation in the Monte Carlo simulation. It is known that location \vec{r} in the raw coordinate system becomes \vec{r}' in the new system, and unit directional vector \vec{s} in the raw coordinate system becomes \vec{s}' in the new system. The problem is to transform arbitrary vector \vec{v} from the raw system to the new system. This can be achieved by rotating \vec{v} by π about the midaxis of \vec{s} and \vec{s}' , then translating

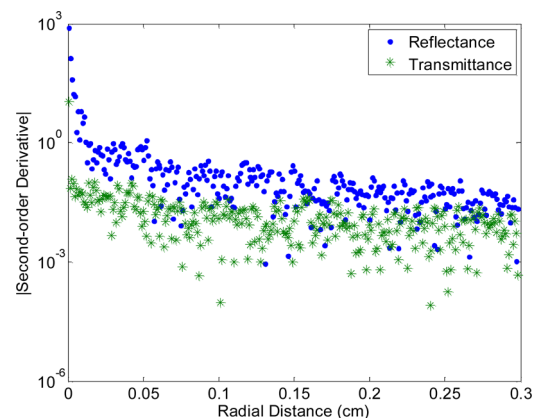


Fig. 6. (Color online) Absolute values of the second-order derivatives of the reflectance and the transmittance as a function of the radial distance. The optical properties of the simulation that generated the result are shown in Table 2.

by $\vec{r}' - \vec{r}$. Assume the midaxis of \vec{s} and \vec{s}' is $(\vec{s} + \vec{s}')/2$, which becomes $\hat{n} = (x, y, z)$ after being normalized to unity length. Then the transformation matrix becomes

$$M(\hat{n}, \pi) = \begin{bmatrix} -1 + 2x^2 & 2xy & 2xz \\ 2xy & -1 + 2y^2 & 2yz \\ 2xz & 2yz & -1 + 2z^2 \end{bmatrix}. \quad (\text{A2})$$

So the transformed vector should be

$$\vec{v}' = M(\hat{n}, \pi) \cdot (x, y, z)^T + \vec{r}' - \vec{r},$$

where T indicates the matrix transpose operation.

Appendix B

The procedure for calculating the modulated light intensity when the exit location change is induced by the variation of the total attenuation coefficient or refractive index is as follows:

1. Assume a finite ring detector. Take the average of all photons collected by this detector to obtain the polynomial fits for the following parameters as a function of the radial distance:

- a. Fraction of detected photons per unit thickness of the ring detector: $F(r)$
- b. Mean weight of detected photons: $W(r)$
- c. Mean path length of detected photons: $L(r)$
- d. $\cos(\omega_a t)$ coefficient of the change in r : $\Delta r_c(r)$
- e. $\sin(\omega_a t)$ coefficient of the change in r : $\Delta r_s(r)$

2. For a certain time point, t , a thickness of the ring detector, D , and the distance from the origin, d , find the range of r , say r_1 to r_2 , so the modulated exit location is within the ring detector, i.e.,

$$\begin{aligned} d - D/2 < r + \Delta r_c(r) \cdot \cos(\omega_a t) + \Delta r_s(r) \cdot \sin(\omega_a t) \\ < d + D/2, \end{aligned} \quad (\text{B1})$$

then $r_1 = d - D/2 - \Delta r_c(r_1) \cdot \cos(\omega_a t) - \Delta r_s(r_1) \cdot \sin(\omega_a t)$ and $r_2 = d + D/2 - \Delta r_c(r_2) \cdot \cos(\omega_a t) - \Delta r_s(r_2) \cdot \sin(\omega_a t)$. This is equivalent to finding the roots of the following polynomial equations:

$$\begin{aligned} \Delta r_c(r) \cdot \cos(\omega_a t) + \Delta r_s(r) \cdot \sin(\omega_a t) \\ + r - (d - D/2) = 0, \end{aligned}$$

$$\begin{aligned} \Delta r_c(r) \cdot \cos(\omega_a t) + \Delta r_s(r) \cdot \sin(\omega_a t) \\ + r - (d + D/2) = 0. \end{aligned} \quad (\text{B2})$$

Because $\Delta r_c(r)$ and $\Delta r_s(r)$ are several orders of magnitudes smaller than r , the changes in these coefficients would be much smaller than the change in

r , which ensures that the radial distance range from r_1 to r_2 exactly covers all r , satisfying Eq. (B1).

3. Integrate the intensity of photons collected by the ring detector over $[r_1, r_2]$, i.e.,

$$\int_{r_1}^{r_2} F(r) \cdot W(r) dr. \quad (\text{B3})$$

4. Repeat Steps 2 and 3 for every t to obtain the time-resolved intensity. Then take a Fourier transform of the time-resolved intensity to find the power density at the first-order ultrasonic frequency and the zero frequency. Take the ratio of the two values to get the modulation depth.

The procedure for calculating the intensity with the amplitude change induced by the variation in albedo is similar except that $W(r)$ is time-dependent while r_1 and r_2 are not. In addition, a circular detector whose area is a fraction of the corresponding ring detector was used to closely mimic physical detectors. Specifically the following steps need to be modified: In Step 2, $r_1 = d - D/2$ and $r_2 = d + D/2$. And in Step 3 the intensity of photons collected by a circular detector is integrated over $[r_1, r_2]$, i.e.,

$$\int_{r_1}^{r_2} F(r) \cdot W(r) \cdot S(r) dr. \quad (\text{B4})$$

$S(r)$ is a scaling factor accounting for the conversion from a ring detector to the corresponding circular detector, which can be expressed by the following expression:

$$\begin{aligned} S(r) = \frac{\cos^{-1}\left(\frac{d^2 + r^2 - D^2/4}{2dr}\right)}{\pi}, \quad \text{when } r_1 < r < r_2; \\ \text{otherwise } S(r) = 0. \end{aligned} \quad (\text{B5})$$

References

1. L. V. Wang, "Ultrasound-mediated biophotonic imaging: a review of acousto-optical tomography and photo-acoustic tomography," *Dis. Markers* **19**, 123–138 (2003).
2. W. Leutz and G. Maret, "Ultrasonic modulation of multiply scattered light," *Physica B* **204**, 14–19 (1995).
3. S. Sakadzic and L. V. Wang, "Modulation of multiply scattered coherent light by ultrasonic pulses: an analytical model," *Phys. Rev. E* **72**, 036620 (2005).
4. S. Sakadzic and L. V. Wang, "Ultrasonic modulation of multiply scattered coherent light: an analytical model for anisotropically scattering media," *Phys. Rev. E* **66**, 026603 (2002).
5. L. V. Wang, "Mechanisms of ultrasonic modulation of multiply scattered coherent light: a Monte Carlo model," *Opt. Lett.* **26**, 1191–1193 (2001).
6. M. Kempe, M. Larionov, D. Zaslavsky, and A. Z. Genack, "Acousto-optic tomography with multiply scattered light," *J. Opt. Soc. Am. A* **14**, 1151–1158 (1997).
7. A. Lev and B. Sfez, "In vivo demonstration of the ultrasound-modulated light technique," *J. Opt. Soc. Am. A* **20**, 2347–2354 (2003).

8. S. Sakadzic and L. V. Wang, "High-resolution ultrasound-modulated optical tomography in biological tissues," *Opt. Lett.* **29**, 2770–2772 (2004).
9. A. Lev and B. G. Sfez, "Direct, noninvasive detection of photon density in turbid media," *Opt. Lett.* **27**, 473–475 (2002).
10. S. Leveque-Fort, J. Selb, L. Pottier, and A. C. Boccara, "In situ local tissue characterization and imaging by backscattering acousto-optic imaging," *Opt. Commun.* **196**, 127–131 (2001).
11. Y. Gang, J. Shuliang, and L. V. Wang, "Frequency-swept ultrasound-modulated optical tomography in biological tissue by use of parallel detection," *Opt. Lett.* **25**, 734–736 (2000).
12. L. Sui, R. A. Roy, C. A. DiMarzio, and T. W. Murray, "Imaging in diffuse media with pulsed-ultrasound-modulated light and the photorefractive effect," *Appl. Opt.* **44**, 4041–4048 (2005).
13. M. Atlan, B. C. Forget, F. Ramaz, A. C. Boccara, and M. Gross, "Pulsed acousto-optic imaging in dynamic scattering media with heterodyne parallel speckle detection," *Opt. Lett.* **30**, 1360–1362 (2005).
14. G. D. Mahan, W. E. Engler, J. J. Tiemann, and E. Uzgiris, "Ultrasonic tagging of light: theory," *Proc. Natl. Acad. Sci. USA* **95**, 14015–14019 (1998).
15. E. Granot, A. Lev, Z. Kotler, B. G. Sfez, and H. Taitelbaum, "Detection of inhomogeneities with ultrasound tagging of light," *J. Opt. Soc. Am. A* **18**, 1962–1967 (2001).
16. K. B. Krishnan, P. Fomitchov, S. J. Lomnes, M. Kollegal, and F. P. Jansen, "A theory for the ultrasonic modulation of incoherent light in turbid medium," in *Optical Methods in Drug Discovery and Development*, M. Analoui and D. A. Dunn, eds. (International Society for Optical Engineering, 2005), p. 60090.
17. M. Kobayashi, T. Mizumoto, Y. Shibuya, M. Enomoto, and M. Takeda, "Fluorescence tomography in turbid media based on acousto-optic modulation imaging," *Appl. Phys. Lett.* **89**, 181101 (2006).
18. L. V. Wang, "Mechanisms of ultrasonic modulation of multiply scattered coherent light: an analytic model," *Phys. Rev. Lett.* **87**, 043903 (2001).
19. A. Sassaroli and S. Fantini, "Comment on the modified Beer–Lambert law for scattering media," *Phys. Med. Biol.* **49**, N255–N257 (2004).
20. R. Graaff, J. G. Aarnoudse, J. R. Zijp, P. M. A. Sloot, F. F. M. de Mul, J. Greve, and M. H. Koelink, "Reduced light-scattering properties for mixtures of spherical particles: a simple approximation derived from Mie calculations," *Appl. Opt.* **31**, 1370–1376 (1992).
21. M. Born and E. Wolf, *Principles of Optics: Electromagnetic Theory of Propagation, Interference and Diffraction of Light* (Cambridge University, 1999).
22. S. J. Norton and M. Linzer, "Correcting for ray refraction in velocity and attenuation tomography: a perturbation approach," *Ultrason. Imag.* **4**, 201–233 (1982).
23. L. Wang, S. L. Jacques, and L. Zheng, "MCML—Monte Carlo modeling of light transport in multi-layered tissues," *Comput. Methods Programs Biomed.* **47**, 131–146 (1995).
24. Y. Gang and L. V. Wang, "Theoretical and experimental studies of ultrasound-modulated optical tomography in biological tissue," *Appl. Opt.* **39**, 659–664 (2000).
25. T. J. Farrell, M. S. Patterson, and B. Wilson, "A diffusion theory model of spatially resolved, steady-state diffuse reflectance for the noninvasive determination of tissue optical properties in vivo," *Med. Phys.* **19**, 879–888 (1992).
26. T. Khan and J. Huabei, "A new diffusion approximation to the radiative transfer equation for scattering media with spatially varying refractive indices," *J. Opt. A* **5**, 137–141 (2003).
27. S. Norton, Q. Liu, and T. Vo-Dinh, "Ultrasonic modulation of diffuse incoherent light—a diffuse theory-based model," in preparation (2008).
28. W. Lihong and Z. Xuemei, "Ultrasound-modulated optical tomography of absorbing objects buried in dense tissue-simulating turbid media," *Appl. Opt.* **36**, 7277–7282 (1997).
29. E. W. Weisstein, "Rotation formula," <http://mathworld.wolfram.com/RotationFormula.html>.